Volume 1 | Number 1 | Jan 2013 | Pages 1–100

Nanoscale

www.rsc.org/nanoscale

ROYAL SOCIETY
OF CHEMISTRY

ROYAL SOCIETY
OF CHEMISTRY

www.rsc.org/nanoscale

Nanoscale

ARTICLE

CO₂-Activated, Hierarchical Trimodal Porous Graphene Frameworks for Ultrahigh and Ultrafast Capacitive Behavior

Sol Yun,[a] Sung-Oong Kang,[a] Sungjin Park[b] and Ho Seok Park*[a]

Herein, we demonstrate CO₂-activated macroscopic graphene architectures with trimodal pore systems that consist of 3D inter-networked macroporosity arising from self-assembly, mesoporosity arising from the intervoids of nanosheets, and microporosity *via* CO₂ activation. The existence of micropore residing in hierarchical structures of trimodal porous graphene frameworks (tGFs) contributes to greatly improve the surface area and pore volume, which are ~3.8 times greater than typical values of existing 3D macroporous graphene monoliths. As confirmed by the specific capacity, the kinetic parameters, and the regeneration capability for chemical adsorption as well as the specific capacitance, the rate capability, and the cycle stability for electrochemical energy storage, the tGFs have an ideal texture for high performance capacitive materials. Furthermore, the tGFs obtain the structurally and energetically homogeneous surface active sites, which dominantly operate through the π-π interactions for adsorption. Consequently, the ultrahigh capacitance and ultrafast capacitive performance of the tGFs for both chemical and electrochemical adsorptions are attributed to hierarchical trimodal porosity and surface chemistry. These results offer a chemical approach combining self-assembly with conventional activation for the construction of 3D hierarchical structure with multimodal porosity.

Introduction

Adsorption occurring at the surface of solid is a fundamental phenomenon that is essential to a wide range of applications, such as electrochemical energy storage, gas capture, molecular separation, and environmental remediation.[1-3] For both electrochemical and chemical systems, the specific capacity (i.e. the amount of adsorbate per unit mass of adsorbent) is the most critical parameter for evaluation of adsorbent performance. Except in cases in which the chemical and electrochemical reaction forms chemical bonds, the capacity is proportional to the accessible surface area of adsorbent; the capacity can thus be improved by increasing the surface area, accomplished by either creating microporosity or by reducing the particle size.[4,5] However, this approach is often hampered by deterioration of the adsorption kinetics as a result of concentration polarization (for both chemical and electrochemical systems) arising from slowed mass and ion transport.[6,7] The use of micropores to create large surface areas in carbonaceous materials for electrochemical energy storage can also result in decreased electronic conductivity due to additional defect formation. In

conjunction with high electronic conductivity (particularly for electrochemical systems, this allows fast charge-discharge rate) and (electro)chemical stability (this allows high cyclic performance over long lifetimes), the most important property for the development of an advanced adsorbent with ultrahigh capacity and ultrafast capacitive performance is hierarchical multimodal porosity. This type of porosity integrates macro-(>50 nm pore size) and meso-porosity (2 to 50 nm pore size) for fast kinetics and microporosity (<2 nm pore size) for high capacity.[6-10] Considering the academic and real-world impact of the trimodal porous inorganic materials previously reported in the literatures,[11,12] multimodal porous graphenes would certainly be considered advanced capacitive materials.

Physical and chemical activation is a conventional technology to achieve microporosity in porous carbons by enlarging the surface area.[13] Such existing techniques have been revisited in the nanotechnology and graphene literature since dramatic capacitance enhancements in KOH-activated graphenes were demonstrated, due to increased available surface area.[14,15] Nevertheless, microporous graphenes neither exhibit fast mass and ion transport kinetics nor provide easy

access to adsorption sites. Given that three-dimensional (3D) interconnected macroporosity is needed to resolve these issues,[8-10] hierarchical porosity is hypothesized to be an ideal texture for high performance capacitive materials. Moreover, capacitive materials need to be assembled into a monolithic form on a bulk level for most practical applications.

Another important issue in graphene chemistry is assembly into 3D macrostructures with interconnected pathways for facilitated mass and ion transport.[16,17] 3D macroporous graphene frameworks are extremely attractive because they allow synergy between the advantages of the 3D macrostructure and the constitutive graphene skeletons: a hierarchical structure provides macroporous accessible areas, allowing easy ion accessibility, fast electron transport, and low-resistance to ion diffusion,[18-20] while graphene nanosheets offer high electrical conductivity, large surface area, and electrochemical and mechanical stability.[21-24] However, the surface area diminishes as the pore size increases up to the scale of macropores. Consequently, the textural properties of conventional 3D graphene monoliths are limited to surface areas of 200 m^2/g,[25] which could be overcome using supercritical drying with the disadvantage of extreme conditions and high cost.[26] Despite extensive effort put forth by the community on the development of porous graphene and 3D architectures,[16,17,25,26] 3D graphene monoliths with hierarchical trimodal porosity have yet to be explored. Herein, we demonstrate CO_2-activated macroscopic graphene architectures with hierarchical trimodal pore systems that consist of 3D inter-networked macroporosity arising from self-assembly, mesoporosity arising from the intervoids of nanosheets, and microporosity *via* CO_2 activation.

Experimental

Synthesis of hierarchical trimodal porous graphene frameworks

The graphene frameworks (GFs) were synthesized following the previous method.[27] GFs were prepared by a combined chemical reduction assembly and freeze-drying process. 1 mg mL^{-1} of an aqueous graphene oxide (GO) dispersion was mixed with hypophosphrous acid (H_3PO_2) and iodine (I_2) (weight ratio of aquous GO solution:H_3PO_2:I_2 is 1:100:10) in a cylindrical vial. The resulting mixture was thermally treated at 80 °C for 8 hour. After gel formation, the reduced graphene oxide (rGO) wet-gel was taken out, washed until pH 7, and freeze-dried into the GF aerogels. The GFs was heated to stabilize at 500 °C for 3 hour in a horizontal tube furnace, with an N_2 flow of 100 sccm. The temperature was ramped from room temperature to 500 °C at a heating rate of 5 °C min^{-1}. After an immediate stabilization, the temperature was continuously raised to 900 °C at a heating rate of 5 °C min^{-1} and then, gas flow exchanged from N_2 to CO_2. The stabilized GFs were activated at 900 °C for 1 hour by CO_2 gas. After CO_2 activation, the temperature remained constant for 1 hour with N_2 flow of 100 sccm and then, cooled down under ambient conditions. The as-obtained trimodal porous graphene frameworks (tGFs) was characterized and applied into chemical adsorption, and electrochemical capacitor (EC).

Application into chemical adsorption

The organic solvent adsorption capacities were determined by measuring the weight of each sample. All organic solvents were supplied by Sigma Aldrich. The adsorbents were initially weighed accurately and then, submerged in several organic solvents for 5 min. The saturated sorbents were then taken out of the vial and weighed. Organic adsorption capacity of each sample were calculated as follows: adsorption capacity (g solvent/g adsorbent) = $(M_2 - M_1)/M_1$, where M_1 and M_2 represent the weight of the adsorbent before and after absorption of organic solvent.

For regeneration, the saturated tGFs adsorbing acetone was dried at 80 °C in an oven. The regenerated tGFs was used again for acetone adsorption test. The regeneration capability of the GFs was investigated after the aceton adsorption test follwing the same procedure as 1st adsorption. The acetone adsorption using regenerated tGFs served as a basis for evaluation of the regeneration efficiency.

Methylene blue (supplied by Sigma Aldrich) was used as an adsorbate. A methylene blue solution was prepared with deionized (DI) water. For adsorption test, each adsorbents were added into methylene blue solutions at a desired concentration. The dye solution was separated from the adsorbent. The concentration of methylene blue in the dye solution before and after adsorption was determined using Ultraviolet-visible spectrophotometer (UV-Vis, JASCO V-570) at 664nm.

Application into electrochemical capacitor

The cyclic voltammetry (CV) and galvanostatic charge/discharge (GCD) measurements were carried out using a three electrode system. Each sample was used as a working electrode, Ag/AgCl as reference electrode, and Pt wire as a counter electrode. 1 M of aqueous H_2SO_4 solution was used as an electrolyte. All potentials were referred to Ag/AgCl reference electrode. The electrochemical characteristics were evaluated using a CHI 760D Electrochemical Workstation (CH Instruments) at room temperature. A symmetric two electrode configuration was assembled following our previous work.[28] The active materials used as a current collector were prepared by slicing tGFs into two pieces with the same mass. A Whatman glass microfiber filter used as the separator was immersed in 1 M of aqueous H_2SO_4 solution. The symmetric devices were configured sandwiching aqueous-electrolyte-soaked separator between two tGFs and clamped for a good contact.

Results and discussion

The hierarchical trimodal porous graphene frameworks (tGFs) in this study was readily achieved through self-assembly and CO_2 activation, as detailed in Fig. 1. Graphene oxides (GOs) obtained from a modified Hummers' method were used as a starting material for the CO_2-activated tGFs.[28,29] GOs were well-dispersed in an aqueous solution, an extremely crucial step for the formation of a 3D networked structure *via* self-assembly.

The organization and assembly into 3D reduced graphene oxide (RGO) hydrogels was driven by π-π stacking interactions of the conjugated structure during the hydrothermal reaction process.[30] The GFs were achieved by freeze-drying the resulting hydrogel to preserve its 3D macroporosity, followed by conversion to tGFs by CO_2 activation. In order to enlarge the surface area and to provide additional porous structure, we chose to physically activate the GFs with CO_2 at high temperature (typically above 800 °C), because it is simpler, safer, and cleaner than chemical activation, which requires washing with hazardous chemicals. Chemical activation using KOH and H_3PO_4 was also attempted, but it was found that the 3D macroporosity was destroyed by the harsh chemical reactions. The final product was obtained as a monolithic column with a density of 7.43 mg cm^{-3}, a diameter of 0.76 cm, and a height of 0.8 cm and its dimension could be controlled by the size of hydrothermal reactor.[30] The 3D macroscopic networked structure of the tGFs was preserved because of the mechanical integrity of graphene pore walls and the mild activation chemistry.
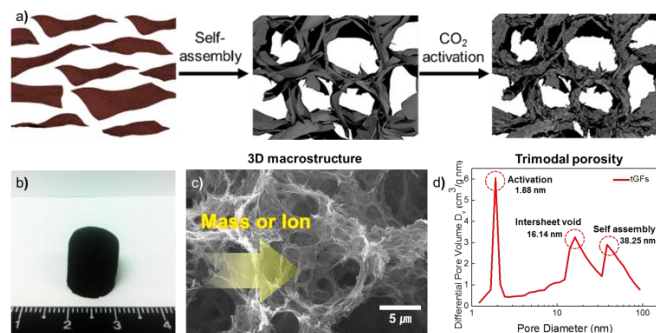

Fig. 1 (a) Schematic illustration of preparing for the tGFs through a self-assembly and CO_2 activation. (b) Optical image of the resultant tGFs. (c) Concept of fast mass and ion transport through a continuous macroporous pathway. (d) Micro- and meso-porosity of the tGFs and its origin.

The morphologies of tGFs were investigated by scanning electron microscopy (SEM) and transmission electron microscopy (TEM). The monolithic tGFs revealed the 3D interconnected macroscopic structures, in which the pore walls were composed of CO_2-activated RGO nanosheets, as observed by SEM images (Fig. 2a). The macroporosity of the 3D GFs remained intact even after CO_2 activation at high temperature (900 °C). The macropores of the tGFs with a diameter ranging from several μm to larger than 10 μm were observed. The existence of mesopores could be visualized in a high-magnification SEM image, whereas very small dark spots might be associated with the existence of micropores (Fig. 2b). The microporosity of the tGFs were further identified by the high-resolution (HR)-TEM image, which showed the micropores (corresponding to dark spots) with a diameters smaller than 2 nm residing on the nanosheets (Fig. 2c). In order to confirm the presence of micro- and meso-porosity of the tGFs, their textural properties are characterized by N_2 adsorption/desorption isotherms (Fig. 2d). A typical type-IV isotherm curve of tGFs with hysteresis corresponds to the existence of mesopores. The mesopores of 16 nm, originating from the intervoids of RGO sheets were clearly observed by BET analysis. Importantly, the surface area and pore volume of the tGFs were dramatically increased to 829.0 m^2 g^{-1} and 2.829 cm^3 g^{-1}, respectively, ~3.8 times greater than typical values of 3D macroporous RGO monoliths (214.8 m^2 g^{-1} and 0.750 cm^3 g^{-1}, respectively) (Table 1). These values are much higher surface area than those of conventional 3D RGO monoliths.[25,26] As evaluated by N_2 adsorption/desorption isotherms, the surface areas of tGFs arising from micro- and meso-pores were estimated to be 21.1 % and 78.9 % of the total measured area, respectively, while those of GFs were 10.7 % and 89.3 %, respectively. The super-microporous regime ranging > 2 nm of pore size was the largest contributor to the enlarged surface area (462.4 m^2 g^{-1} increase), also increasing the proportion of the microporous regime absolutely. These results indicate that
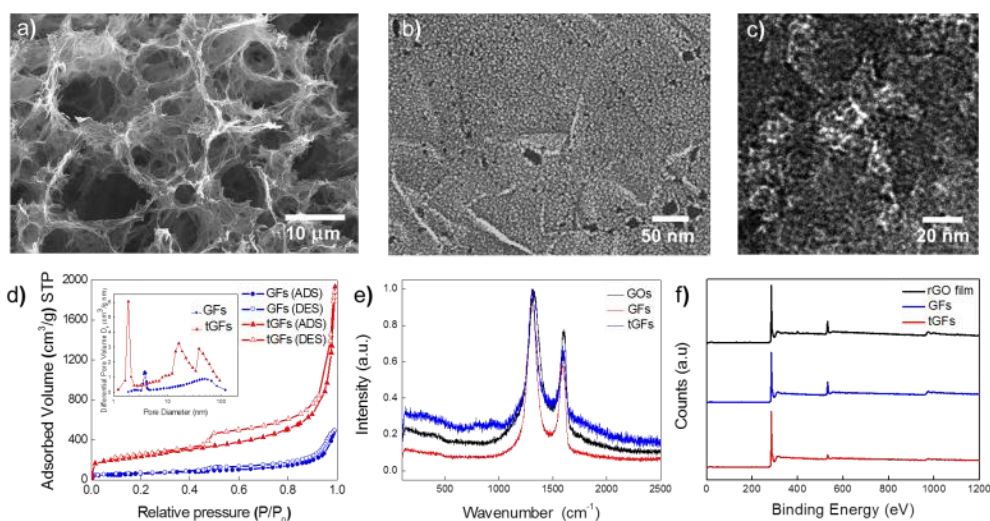

Fig. 2 Characterization of tGFs. (a) Low- and (b) high-magnificent SEM and (c) HR-TEM images of tGFs. (d) N_2 adsorption/desorption isotherms of AC, RGO, GF, and tGF. Inset is BJH pore size distribution of GF and tGF. e) Raman spectra of GO, GF, and tGF. (f) Full scans of XPS curves of RGO, GF, and tGF.

Table 1. BET surface area and pore volume of GFs and tGFs at respective micropore and mesopore region.

Sample	Total surface area [m^2/g]	Surface area (in meso regime) [m^2/g]	Surface area (in micro regime) [m^2/g]	Total pore volume [cm^3/g]
GFs	214.8	191.9 (89.3%)	22.9 (10.7%)	0.750
tGFs	829.0	654.3 (78.9%)	174.7 (21.1%)	2.829

CO_2 activation led to enlargement of the surface area in the microporous regime by 151.8 m^2 g^{-1} (660 % increase). The existence of micropores created by CO_2 activation was also verified by an increase in the quantity of N_2 gas adsorbed at the low relative pressure of < 0.1, corresponding to the microporous regime. Notably, trimodal porous structure of tGFs was confirmed by three peaks of the BJH pore size distribution centered at 1.88 nm, 16.14 nm, and 38.25 nm (marked by red arrows in Fig. 1d) and SEM image (Fig. 1c); GFs showed bimodal pore systems typical for macroporous RGOs.[31] This is the first demonstration of a hierarchical trimodal porosity in 3D graphene monoliths, which could be accomplished by the construction of an additional pore system by CO_2 activation. The formation mechanism of the micropore by CO_2 activation which is beyond the scope of this research needs to be further studied as a future work. In our system, an hour of CO_2 activation at 900 °C were determined to be the optimum conditions because the macroporosity was degraded by CO_2 activation either for longer time or at higher temperature. The microscopic wrinkled structure and rough surface of the tGFs was evinced by TEM images (Fig. S1 in ESI†). Such the corrugated and crumpled tGF sheets can provide larger accessible area compared to graphene powder, which highlights the impact of CO_2 activation on the morphological feature.

The chemical structure of the tGFs was investigated by Raman and x-ray photoelectron spectroscopy (XPS). In Raman spectra of graphitic carbons, the intensity ratio of the D-band to the G-band (I_D/I_G) is regarded as an indicator of the degree of conjugation destruction, because the D- and G-bands at 1310 and 1590 cm^{-1} are attributed to disordered graphene layers and tangential C-C stretching vibrations, respectively.[32] The I_D/I_G of the tGFs was comparable to that of the GFs, indicating that despite the formation of micropores by CO_2 activation, the intrinsic conjugated structure related to the electrical properties was not significantly damaged (Fig. 2e).[14,15] The chemical identity and circumstances of the tGFs are confirmed by XPS analysis (Fig. 2f and Fig. S2 in ESI†). Along with similar values of I_D/I_G before and after CO_2 activation, the measured decrease in oxygen content indicates a thermal reduction without significant damage to the conjugated structure during CO_2 activation.

The superiority of the tGFs is demonstrated here by application to adsorption and energy storage. First, organic solvents and dyes were adsorbed to evaluate the adsorption kinetics and capacity of the tGFs. We used activated carbon (AC, a commercial product) and GFs as control samples. In order to emphasize the importance of trimodal porosity on kinetics, the adsorption behavior was tested at a neutral condition (pH of 7.6) using methylene blue as a model dye adsorbate. The plot of time (t) vs. capacity (q_t, normalized by maximum value) was fitted to the following pseudo-2nd order adsorption kinetic equation (Fig. 3a): $t/q_t = 1/kq_e^2 + (1/q_e)t$. The rate constants ($k$) of ACs, GFs, and tGFs obtained from the slope of the plot were calculated as 0.90×10^{-3} g mg^{-1} min^{-1}, 0.97×10^{-3} g mg^{-1} min^{-1}, and 1.4×10^{-3} g mg^{-1} min^{-1}, whereas the half-life times ($t_{1/2}$) calculated by the intercept of the plot were
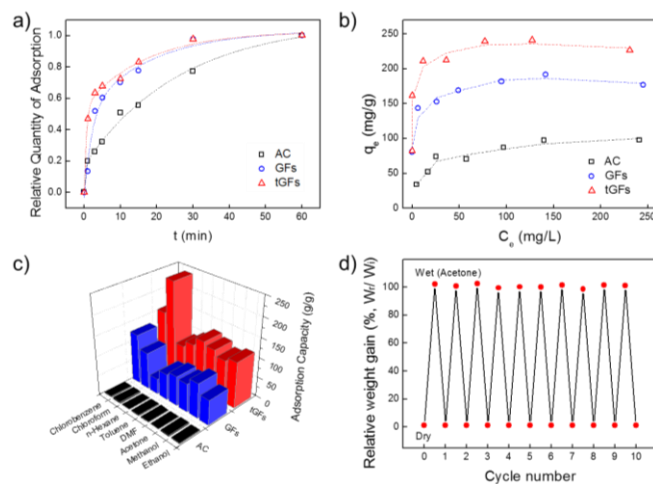

Fig. 3 Chemical adsorption properties of tGFs. (a) Plots of time (t) vs. corresponding capacity (normalized by maximum value) of AC, GF, and tGF for adsorption of methylene blue at a pH of 7.6. (b) Plots of equilibrium concentration (C_e) vs. equilibrium capacity (q_e) of Ac, GF, and tGF for adsorption of methylene blue. (c) Adsorption capacities of AC, GF, and tGF for chlorobenzene, chloroform, n-hexane, toluene, dimethylformamide, acetone, methanol, and ethanol. (d) Regeneration curves of tGF for adsorption of acetone.

Table 2. Langmuir isotherm and pseudo-2nd order kinetic parameters for removal of methylene blue by AC, GFs, and tGFs

Pseudo-2nd order constants	k (g/mg min)	$t_{1/2}$ (min)	R^2
AC	8.9219E-4	11.20	0.9630
GFs	9.7364E-4	5.03	0.9945
tGFs	1.4059E-3	2.61	0.9968
Langmuir constants	K (dm^3/mg)	q_{max} (mg/g)	R^2
AC	0.0646	104.1667	0.9932
GFs	0.9016	181.8182	0.9967
tGFs	31.7995	230.4147	0.9985

11.20 min, 5.03 min, and 2.61 min, respectively (Table 2 and Fig. S3 in ESI†). The adsorption kinetics of the tGFs was much faster than that of AC due to the 3D interconnected macroporous pathways and even faster than the GFs. As demonstrated by Langmuir isotherms of the three samples for the adsorption of methylene blue (Fig. 3b), the adsorbent-adsorbate interactions were the most favourable for the tGFs, shown by its higher slope of saturation curve and larger Langmuir constant (K) in the following equation: $C_e/q_e = C_e/q_{max} + 1/Kq_{max}$ (Table 2 and Fig. S4 in ESI†). Along with the trimodal textures of the tGFs, their surface properties made them suitable for the adsorption of organic solvents and dyes. Accordingly, the capacities of the AC, GF, and tGF were compared by measuring the adsorption capacities of a broad range of organic solvents, including chlorobenzene, chloroform, n-hexane, toluene, dimethylformamide, acetone, methanol, and ethanol (Fig. 3c and Table S1 in ESI†). As a result of the enlarged surface area and favourable surface chemistry, the tGFs showed greater capacities than the GFs, irrespective of the chemical identity of the organic solvent. In particular, the capacities of both the GFs and the tGFs were two orders of magnitude greater than those of ACs, indicating that hierarchical porosity was significant for the capture of organic solvents. In addition to the improved adsorption capacity and kinetics, the tGFs exhibited an excellent regeneration capability of ~100 % as demonstrated by at least 10 adsorption/desorption cycles of acetone for more practical applications (Fig. 3d).

In order to understand the surface chemistry and morphology of the tGFs, the adsorption isotherms and kinetics need to be discussed further. As previously reported for the adsorption of organic dye, the active adsorption sites of the tGFs consist of (i) delocalized sp^2 conjugated π electrons interacting with either the lone electron pairs of atoms or the free electrons in the aromatic rings of the dye molecules and (ii) negatively charged surface hydroxyl (-OH) and carboxyl (-

COOH) functional groups in an aqueous solution.[33,34] Given the chemical structure of methylene blue and pseudo-2nd order kinetics, the tGFs are able to capture dye molecules in two types of interactions: (i) through π-π interactions between the conjugated aromatic rings of the tGFs and the dye molecules and (ii) through electrostatic attraction between the dye's positively-charged amino groups and the tGF's negatively-charged oxygen-containing surface groups. Considering the more favourable binding methylene blue to the tGFs (derived from the higher Langmuir constant and the lower oxygen content, K=31.80 and C/O=4.39) rather than those of AC (K=0.06) and GF (K=0.90 and C/O=2.44), it is worth noting that the π-π interaction is more dominating factor over electrostatic attraction for dye adsorption. In particular, it can be inferred that the adsorption sites of the GFs are uniformly distributed, because their adsorption behaviour followed the Langmuir isotherm model corresponding to the adsorption on structurally and energetically homogeneous active sites.[35]

We next applied tGFs into electrochemical systems to take full advantages of their good electrical and textural properties. The electrochemical and capacitive behaviors of the tGFs were evaluated by cyclic voltammetry (CV) and galvanostatic charge/discharge (GCD) curves. The measurement was made in an aqueous 1 M H_2SO_4 electrolyte in a three-electrode configuration. RGO films were used as a control sample to evaluate the effect of the 3D macroporosity on electrochemical capacitive behavior. In CV curves at a rate of 5 mV s^{-1}, RGO films, 3D GFs and tGFs exhibited a rectangular shape, indicating near-ideal double layer capacitive behavior (Figs. 4a, 4b, and 4c). Moreover, a symmetric triangular shape of three samples in GCD curves was in a good line with typical double layer capacitive feature of CV curves (Fig. 4d). The specific capacitance (C_S) values of RGO and GFs were 153.0 and 157.7 F g^{-1}, respectively, in reasonable agreement with values from previous studies.[36] On the other hand, the C_S of tGFs (278.5 F
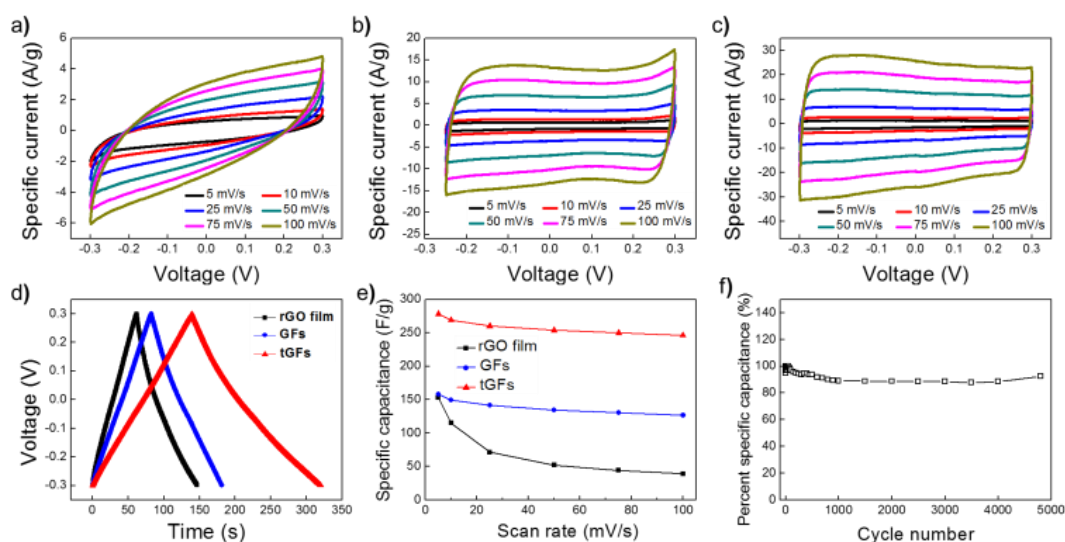

Fig. 4 Electrochemical capacitive properties of tGFs. CV curves of (a) RGO, (b) GF, and (c) tGF at the scan rates of 1 mV s^{-1} to 100 mV s^{-1}. (d) GCD curves of RGO, GF, and tGF at 1 A g^{-1}. (e) Rate capabilities of RGO, GF, and tGF at a scan rate of 5 − 100 mV s^{-1}. (f) Cyclic performances of tGF during 5,000 charge/discharge cycles at a specific current of 5 A g^{-1}. All tests were performed in 1M of aqueous H_2SO_4 solutions.

g^{-1}) was improved by more than 175% of the RGO and GFs. The advantage of 3D macroporosity became more pronounced when the tGFs were charged at high rates. As the scan rate was increased 20-fold from 5 to 100 mV s^{-1}, the CV curves of the GFs and tGFs maintained a rectangular shape, indicative of the low ionic resistance at high rates (Fig. 4e and Fig. S5 in ESI†). However, the CV curve of RGOs was significantly distorted, resulting in a dramatic decrease of the capacitance to 39.0 F g^{-1}. Even with a 2-fold higher capacitance due to enlarged surface area by CO_2 activation, the tGFs showed a capacitance retention of 88.5 %, greater than the 25.5 % of the RGOs and 80.2 % of the GFs, respectively. The capacitance values of three samples measured by GCD curves ranging from 1 A g^{-1} to 10 A g^{-1} showed the same trends as those by CV curves in spite of slight discrepancy due to different measurement conditions (Fig. S6 in ESI†). The fast ion transport of tGFs through the 3D continuous pathways, which is associated with good rate capability, is evinced by a steep Warburg-type line of Nyquist plot at the low frequency, resulting in a more ideal capacitive feature rather than RGO (Fig. S7 in ESI†). This finding highlights the role of a hierarchically, inter-networked trimodal porosity in the capacitance improvement and retention for the good electrochemical capacitive performances.

For more practical application, we measured the cyclic stability of the tGFs using GCD curves in a symmetric two-electrode configuration (Fig. 4f). As a consequence of the internal resistance of cell configuration, the initial value in a two-electrode configuration was slightly lower than values obtained from CV curves in a three electrode configuration, which can be resolved by optimizing device components and assembly. After 5,000 charge/discharge cycles at a specific current of 5 A g^{-1}, which shows both cyclic and rate capabilities, the capacitance retention of the tGFs was 92.2 % of initial capacitance. Even with a higher capacitance and rate capability, the tGFs exhibited better cyclic stability than GAs at high scan rates. The CV curve of the tGFs exhibited good capacitive behavior due to highly reversible charge storage and mechanical integrity.

Conclusions

We have demonstrated the preparation of 3D, hierarchical trimodal porous GFs through self-assembly and CO_2 activation. The ultrahigh capacitance and ultrafast capacitive performance of the tGFs under both chemical and electrochemical adsorption conditions were attributed to hierarchical trimodal porosity, consisting of macropores (constructed by self-assembly of graphene sheets) and micro- and mesopores (achieved by CO_2 activation). The reversible cycling ability of the tGFs in both chemical and electrochemical adsorptions was due to the mechanical and (electro)chemical stabilities of the macrostructure and its constitutive graphene nanosheets. This result offers a chemical approach combining self-assembly with conventional activation for the construction of 3D hierarchical structure with multimodal porosity using low-dimensional carbon nanomaterials.

Notes and references

[a] Department of Chemical Engineering, College of Engineering, Kyung Hee University, 1 Seochon-dong, Giheung-gu, Youngin-si, Gyeonggi-do 446-701, Republic of Korea

E-mail: phs0727@khu.ac.kr

[b] Department of Chemistry, Inha University, Incheon 402-751, Republic of Korea

† Electronic Supplementary Information (ESI) available: Characterization, TEM, high resultion XPS, plots of pseudo-2nd order kinetics and Langmuir isotherms, CV and GCD curves, Nyquist plots, and adsorption capacities. See DOI: 10.1039/b000000x/

1. B. E. Conway, Electrochemical Supercapacitors: Scientific Fundamentals and Technological Applications, Kluwer Academic/Plenum, New York, 1999

2. I. Ali, *Chem. Rev.*, 2012, **112**, 5073−5091.

3. K. Yang and B. Xing, *Chem. Rev.*, 2010, **110**, 5989–6008.

4. M. Behl, J. Yeom, Q. Lineberry, P. K. Jain and M. A. Shannon, *Nat. Nanotech.*, 2012, **7**, 810–815.

5. P. Balaya, *Energy Environ. Sci.*, 2008, **1**, 645–654.

6. B. L. Su, C. Sanchez and X. Y. Yang, Hierarchically Structured Porous Materials: From Nanoscience to Catalysis, Separation, Optics, Energy, and Life Science, John Wiley & Sons, 2012.

7. R. Liu, J. Duay and S. B. Lee, *Chem. Commun.* 2011, **47**, 1384–1404.

8. P. Simon and Y. Gogotsi, *Nat. Mater.*, 2008, **7**, 845–854.

9. C. Liu, F. Li, L. P. Ma and H. M. Cheng, *Adv. Mater.*, 2010, **22**, E28–E62.

10. D. W. Wang, F. Li, M. Liu, G. Q. Lu and H. M. Cheng, *Angew. Chem. Int. Ed.*, 2008, **120**, 379−382.

11. Y. Ren, Z. Ma, R. E. Morris, Z. Liu, F. Jiao, S. Dai and P. G. Bruce, *Nat. Commun.*, 2013, **4**, doi:10.1038/ncomms3015.

12. S. Lopez-Orozco, A. Inayat, A. Schwab, T. Selvam and W. Schwieger, *Adv. Mater.*, 2011, **23**, 2602–2615.

13. R. C. Bansal, J. B. Donnet and H. F. Stoekcli, In Active Carbon. Marcel Dekker, New York, 1988.

14. Y. Zhu, S. Murali, M. D. Stoller, K. J. Ganesh, W. Cai, P. J. Ferreira, A. Pirkle, R. M. Wallace, K. A. Cychosz, M. Thommes, D. Su, E. A. Stach and R. S. Ruoff, *Science*, 2011, **332**, 1537–1541.

15. L. L. Zhang, X. Zhao, M. D. Stoller, Y. Zhu, H. Ji, S. Murali, Y. Wu, S. Perales, B. Clevenger and R. S. Ruoff, *Nano Lett.*, 2012, **12**, 1806–1812.

16. H. Jiang, P. S. Lee and C. Z. Li, *Energy Environ. Sci.*, 2013, **6**, 41–53.

17. C. Li and G. Q. Shi, *Nanoscale*, 2012, **4**, 5549–5563.

18. M. F. El-Kady, V. Strong, S. Dubin, R. B. Kaner, *Science*, 2012, **335**, 1326–1330.

Nanoscale Accepted Manuscript

19. Z. S. Wu, A. Winter, L. Chen, Y. Sun, A. Turchanin, X. Feng and K. Müllen, *Adv. Mater.*, 2012, **24**, 5130–5135.

20. B. G. Choi, M. Yang, W. H. Hong, J. W. Choi and Y. S. Huh, *ACS Nano*, 2012, **6**, 4020–4028.

21. K. S. Novoselov, A. K. Geim, S. V. Morozov, D. Jiang, Y. Zhang, S. V. Dubonos, I. V. Grigorieva and A. A. Firsov, *Science*, 2004, **306**, 666–669.

22. X. Li, X. Wang, L. Zhang, S. Lee and H. Dai, *Science*, 2008, **319**, 1229–1232.

23. B. G. Choi, H. S. Park, T. J. Park, M. H. Yang, J. S. Kim, S. Y. Jang, N. S. Heo, S. Y. Lee, J. Kong and W. H. Hong, *ACS Nano*, 2010, **4**, 2910–2918.

24. B. G. Choi, J. Hong, Y. C. Park, D. H. Jung, W. H. Hong, P. T. Hammond and H. S. Park, *ACS Nano*, 2011, **5**, 5167–5174.

25. W. Chen, S. Li, C. Chen and L. Yan, *Adv. Mater.*, 2011, **23**, 5679–5683.

26. M. A. Worsley, P. J. Pauzauskie, T. Y. Olson, J. Biener, J. H. Satcher and T. F. Baumann, *J. Am. Chem. Soc.*, 2010, **132**, 14067–14069.

27. H. D. Pham, V. H. Pham, T. V. Cuong, T. D. Nguyen-Phan, J. S. Chung, E. W. Shin and S. Kim, *Chem. Commun.*, 2011, **47**, 9672–9674.

28. B. G. Choi and H. S. Park, *ChemSusChem*, 2012, **5**, 709–715.

29. B. G. Choi, Y. S. Huh, Y. H. Hong, D. Erickson and H. S. Park, *Nanoscale*, 2013, **5**, 3976–3981.

30. Y. X. Xu, K. X. Sheng, C. Li and G. Q. Shi, *ACS Nano*, 2010, **4**, 4324–4330.

31. Z. Xu, Y. Zhang, P. Li and C. Gao, *ACS Nano*, 2012, **6**, 7103–7113.

32. B. G. Choi, W. H. Hong, Y. M. Jung and H. S. Park, *Chem. Commun.*, 2011, **47**, 10293–10295.

33. S. Pei and H. M. Cheng, *Carbon*, 2012, **50**, 3210–3228.

34. D. W. Lee, T. –K. Hong, D. Kang, J. Lee, M. Heo, J. Y. Kim, B. –S. Kim and H. S. Shin, *J. Mater. Chem.*, 2011, **21**, 3438–3442.

35. I. Langmuir, *J. Am. Chem. Soc.*, 1918, **40**, 1361–1403.

36. B. G. Choi, J. Hong, W. H. Hong, P. T. Hammond and H. S. Park, *ACS Nano*, 2011, **5**, 7205–7213.

Nanoscale Accepted Manuscript